Structural, electrical, and dielectric properties of sprayed tungsten-doped ZnO semiconductor

ELHACHEMI ZEHAR[1,*], ABDALLAH OUERDANE[2], BOUALEM CHETTI[2], SAMIHA DERGAL[3,4], TARIK OUAHRANI[4], ALI ÇORUH[5], YVES CAUDANO[6]

[1]*Laboratory of Energy and Smart Systems, Faculty of Science and Technology, University of Khemis Miliana 44225, Algeria*
[2]*University of Khemis Miliana 44225, Algeria*
[3]*Hassiba Ben bouali University, Chlef 02000, Algeria*
[4]*Theoretical Physics Laboratory, Abou Bekr Belkaid University of Tlemcen 13000, Algeria*
[5]*Department of Physics 54147-Kampus Sakarya -Turkey*
[6]*Laboratory Laser and Spectroscopy (LLS) Namur University, Belgium*

The structural, morphological, electrical, and dielectric properties of non-doped ZnO as well as ZnO doped with tungsten were investigated using advanced techniques such as sensitive XRD, XPS spectroscopy techniques, and SEM microscopes. The findings demonstrate that the incorporation of tungsten as a dopant in ZnO leads to enhanced properties characterized by reduced grain size and improved crystal lattice structure. To analyze the electrical and dielectric properties, ohmic contacts on the ZnO interface junctions were established, allowing for comprehensive studies following surface rectification. The task was done by current-voltage (I - V), capacitance-voltage (C - V), conductance-voltage (σ - V), and the real ε' and imaginary ε'' components of the electrical permittivity across a range of voltages and frequencies. All these parameters were carried out using precise network analyzers, covering a voltage range of -6V to + 6V, and a frequency range of 10Hz to 10MHz. The obtained results exhibited outstanding performance, with activation energies measured at 0.49 eV, -0.83 eV, and 0.23 eV, respectively. Furthermore, we observed a significantly high permittivity value of 900 at low frequency, accompanied by distinct I-V characteristics. Notably, the I-V characteristic exhibited a notable increase at 0.6 volts, affirming the exceptional performance of tungsten-doped ZnO (WZO) and its suitability for a wide range of technological applications.

(Received March 9, 2023; accepted August 10, 2023)

Keywords: Structural, Electrical, Dielectrical, Semiconductors

1. Introduction

Among the wide range of metal oxides investigated in the past decade, zinc oxide (ZnO) has garnered significant attention due to its versatile properties. Notably, its non-toxicity, biocompatibility [1], and relatively straightforward and cost-effective synthesis [2] have contributed to its extensive application potential. Moreover, ZnO exhibits excellent physical and chemical stability [3], boasting a wide band gap energy (3.37 eV) and a significant exciton binding energy (60 meV) [4-6]. These exceptional characteristics position ZnO as a semiconductor of choice across various fields, including light-emitting diodes (LEDs) for electromagnetic radiation emission [7-8], laser diodes [9], P.N. and P.I.N. configurations [10-11], photovoltaic cells [12], and photodetectors [13]. Furthermore, ZnO finds relevance in several other applications, such as piezoelectricity [14], thin-film transistors [15], gas sensors [16, 17], biosensors [18], medical applications [19], and supercapacitors for energy storage [20], and display window materials [21]. However, the realization of these technological applications necessitates addressing specific challenges, namely enhancing conductivity, improving electrical mobility, and widening the band gap. However, these properties should be realized through adequate doping. Therefore, chemical elements such as tin (Sn) [22], copper (Cu) [23], indium (In) [24], aluminum (Al) [22, 25], gallium (Ga) [26], tungsten (W) [27], and nickel (Ni) [28] are commonly utilized.

In this work, the use of tungsten (W) for doping zinc oxide is proposed, resulting in the creation of the WZnO material (abbreviated as WZO). By doing so, the high dissociation energy of the oxygen bond with tungsten can improve the retention of oxygen atoms, leading to a decrease in the concentration of oxygen vacancies and an increase in mobility [29]. Preparations of both bare ZnO and doped ZnO (WZO) are then carried out using the spraying pyrolysis technique, which is justified by the fact that the thin films deposited have the same composition as the source material [16, 30-34].

Furthermore, this preparation process was employed to achieve the deposition of large areas with exceptional lateral homogeneity [35]. The resulting thin films were subjected to structural, chemical, morphological, electrical, and dielectric studies. Meanwhile, the phase structure of the thin films was examined using X-ray diffraction (XRD) [36]. To assess the chemical structure and composition of the thin layers, X-ray photoelectron spectroscopy (XPS) was employed [24, 31]. Additionally,

scanning electron microscopy (SEM) was utilized to analyze the surface morphology, confirming the size of the ZnO particles, which could be verified through the XRD technique.

Furthermore, an ohmic contact was established on the ZnO interface. The Schottky junction W-ZnO/p-Si, after surface rectifying, facilitated the investigation of electrical and dielectric properties using techniques such as current-voltage (I–V), capacitance–voltage (C–V), conductance-voltage (σ-V), and real ε' or imaginary ε" components of electrical permittivity for different frequencies.

The development of such a dispositive could provide a means for analyzing the electrical and dielectric parameters using network analyzers within a voltage range of (-6V to +6V) and a frequency range of (10 Hz to 10 MHz) [37-40].

2. Experimental results and discussion

2.1. Preparation of samples

The spray pyrolysis technique is used for the deposition of tungsten-doped ZnO thin films. An aqueous solution is prepared, consisting of high-purity dehydrated powders of zinc acetate and tungsten chloride obtained from Sigma Aldrich. These are substances that are dissolved in ethanol and deionized water. Maintaining a constant deposition rate of 7 ml/min, the precursor solution is atomized by pure compressed air and then sprayed onto a silicon substrate. The substrate is heated to a temperature of 300°C and subsequently raised above 500°C. Notably, the solution contains an estimated atomic concentration of 3% tungsten (W/(Zn+W)). The following chemical reactions represent the successive reactions involved in the synthesis of both pure ZnO and tungsten-doped ZnO [25].

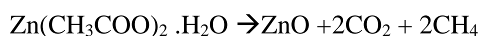

$$Zn(CH_3COO)_2 .H_2O \rightarrow ZnO + 2CO_2 + 2CH_4$$

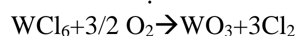

$$WCl_6 + 3/2\ O_2 \rightarrow WO_3 + 3Cl_2$$

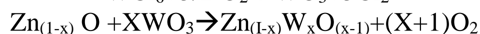

$$Zn_{(1-x)}\ O + XWO_3 \rightarrow Zn_{(I-x)}W_xO_{(x-1)} + (X+1)O_2$$

The thickness measurements of the samples were obtained using a Veecodektak 150 surface profilometer. This system consists of a sample holder, a camera, a lamp, and a diamond tip. A computer-controlled motor system enables precise placement and linear movement of the tip across the surface. The measured thicknesses of the ZnO and WZO thin films were found to be (115±5) nm and (120±5) nm, respectively.

2.2. X-ray diffraction study (XRD)

The crystalline structure of the synthesized undoped Zinc Oxide (UZO) and tungsten Zinc Oxide (WZO) materials was investigated using the X-ray diffraction method (XRD) with a diffractometer system called X'PERT-PRO. The measurements were conducted with CuKα radiation (λ_1 = 1.54060 Å) [41]. The XRD patterns were recorded with a minimum step-size mode (Δ2θ=0.001°) over an angular range from 10.020° to 99.984°. Fig. 1 depicts three peaks identified at the planes (100), (101), and (202), corresponding to Bragg 2θ angles of 31.310°, 35.690°, and 77.374°, respectively. Based on the results, it can be concluded that ZnO crystallizes into the compact hexagonal phase B4 (Würtzite type), as tabulated in the standard JCPDS 80-0075 [42, 43]. Furthermore, the intensity of the (101) peak is notably higher compared to the (100) and (202) lines. Additionally, in Fig. 1, the XRD spectrum of WZO, corresponding to tungsten-doped ZnO matrices, is presented. Fig. 1 and inset 1 demonstrate that the (101) peak in the XRD spectrum shifts from 36.27° for UZO to 36.48° for WZO on the 2θ axis.

Indeed, an angular displacement of 0.21° towards higher Bragg angles and an increase in its intensity compared to pure ZnO are observed. These effects can be attributed to the disparity in the ionic radii of zinc and tungsten ions. [44, 45, 46], The substitution of W^{6+}ions for Zn^{2+} ions in the ZnO lattice induces a structural distortion, resulting in the observed shift towards higher 2θ values. This shift is related to the difference in atomic radii between these ions. Furthermore, the heightened intensity of the WZO peaks can be explained by variations in electronic densities, a phenomenon previously noted by other researchers [46]. The X-ray peak profile analysis (XPPA) allows for the determination of various parameters, such as crystallite size, lattice parameters, lattice strain, lattice stress, and strain energy density. In the case of the ZnO and WZO films, the values of the mesh parameter c and the corresponding DRX peaks of the films ZnO and WZO were found to be 5.178Å and 5.217Å, respectively. These two values closely align with the value of 5.206 Å given by the JCPDS card number 36-1451, corresponding to the compound ZnO [47]. Nevertheless, it is worth noting that the c parameter of the WZO compound displayed an increase compared to the UZO one. This increase is likely a result of tungsten atoms being incorporated into the substitutional sites' Zn in the formed layer [47]. The difference in ionic radii between Zn (0.72 Å) and tungsten (0.60 Å) is evident. The mean grain size (D) was determined by analyzing the widening of the most intense peak corresponding to the diffraction plane (101) using the Debye- Scherer formula [47, 48]:

$$D = \frac{0.9\lambda}{\beta(rd)cos\theta} \quad (1)$$

where D is the grain size, λ is the wavelength of the X-ray, β (rd) is the full width at half the maximum of the peak (101) (FWHM) of ZnO, and θ is the diffraction angle. When applying formula (1) to the XRD peak (101), it is observed that the grain sizes decrease for WZO compared to ZnO, as reported by other authors [49]. The various structural parameters obtained for the two processed samples, UZO and WZO, are summarized in Table I using references that provide corresponding formulas [47, 48]. It

is observed that the WZO crystal undergoes significant changes in algebraic values, exhibiting higher stress and lower strain [50]. However, the strain-to-stress ratio yields a constant value of Y = 453.6 GPa, corresponding to Young's modulus for the deformation of both UZO and WZO crystals. This constant value suggests a proportional relationship between strain and stress, which aligns with the findings of Ref. [51]. The negative sign in strain or stress arises from the direction of atomic deformation within the crystal. Specifically, the lattice tensile strain shifts from +5.570 10^{-3} to -2.119 10^{-3}. The doping process of the ZnO matrix with tungsten leads to reduced resistivity and increased mobility of the charge carriers. These characteristics make WZO a promising material for TFT transistors, as cited in the literature. [52]

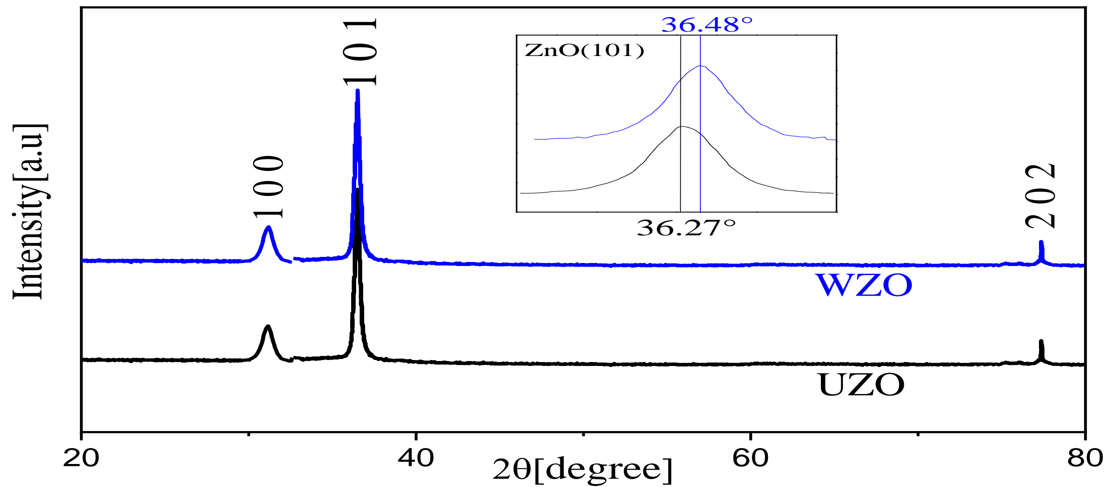

Fig. 1. DRX spectra of Undoped UZO and doped WZO .Inset: peak (101) shifted from 36.27° for ZnO to 36.48° for WZO on 2θ axis, either an angular displacement of 0.21° towards the high Bragg angle (color online)

Table 1. Structural parameters of undoped UZO and doped WZO

	D [nm]	*δ* [$10^{-4}nm^{-2}$]	Lattice parameters [nm]		Strain (ε) (10^{-3})	Stress σ [GPa]	Zn-O [Å]
			a=b	c			
UZO	78	1.6436	3.243	5.178	+ 5.570	-2.526	1.985
WZO	57	3.0778	3.228	5.217	-2.119	0.9612	1.993

2.3. Studies by XPS spectroscopy

The XPS core level survey of ZnO and WZO at the contaminated state (Zn3d, Zn 3p, Zn 3s, Zn 2p, C 1s, O 1s) and Auger transitions (Zn-LMM, W-LMM, O-KLL, and C-KLL) is presented in Fig. 2a. The spectral positions of the XPS were determined using Casa XPS software and calibrated using the fixed value of 284.7 eV for the C1s peaks. Fig. 2b depicts the XPS analysis of the WZO sample, showing the characteristic peaks of the Zn2p doublet corresponding to the oxidation state of Zn^{2+} [32]. The $Zn2p_{3/2}$ and $Zn2p_{1/2}$ components are observed at binding energies of 1022.5 eV and 1045.5 eV, respectively. These binding energies at the $Zn2p_{3/2}$ and $Zn2p_{1/2}$ core levels exhibit slight shifts compared to our previous findings with ZnO-doped cupper [32] and ZnO-doped indium [24]. However, the separation between them is constant and equals 23 eV, which is consistent with the literature [24, 32]. The observed shift of 1.5 eV from the results of Guezzoul [32] and Bedrouni [24] indicates a significant alteration in the oxidation state due to the tungsten doping in ZnO. This indicates that oxidation reactivity is influenced by the presence of metallic elements within the ZnO matrix. Figs. 3a, b, and c display the XPS profiles of W4f in WZO, revealing the presence of two peaks attributed to the division of the spin orbits $W4f_{7/2}$ and $W4f_{5/2}$. The bond energies for $W4f_{7/2}$ and $W4f_{5/2}$ in W metal are around 31.5 eV and 32.5 eV, respectively. In contrast, the bond energies of WO_3 are around 36 and 38 eV [53, 54]. Furthermore, Fig. 3c illustrates a complex O1s profile in the contaminated state. The profiles of the specimen as mixed seem to consist of three spectra: the $O_I$peak corresponds to O^{2-} bonded to Zn^{2+} and represents the stoichiometric phase forming ZnO. The peak O_{II} is associated with O^{2-} ions in the oxygen vacancies and some adsorbed species like hydroxyl (OH) on the surface of the ZnO compound. Finally, the O_{III} peak is attributed to specific chemisorbed oxygen forming H_2O and CO_2. These three peaks have central positions of 528.5, 530, and 532 eV, respectively [24, 29, 55]. To achieve maximum deconvolution, Gaussian functions were employed along with the determination of surface intensities for each resolved spectrum. The reactivity assessment involved a

comparison before and after the heating process. Prior to heating and without etching, the ratios of O_I/O, O_{II}/O, and O_{III}/O were found to be 40.50%, 40.04%, and 14.46%, respectively, indicating the initial proportions. After the heating treatment, the WZO sample was introduced into the preparation chamber and subjected to argon beam bombardment for surface etching. Fig. 3d records the WZO XPS survey in which the binding energies for $W4f_{7/2}$ and $W4f_{5/2}$ were moved towards energies of 37 eV and 39 eV, indicating successful reactivity with ZnO. Furthermore, Fig. 3a displays the emergence of W-NNN peaks at energies of 1168 eV and 1074 eV using an Mg electrode [56]. It is noteworthy that the contamination present on the surface, as observed in the C1s peak, has completely disappeared.

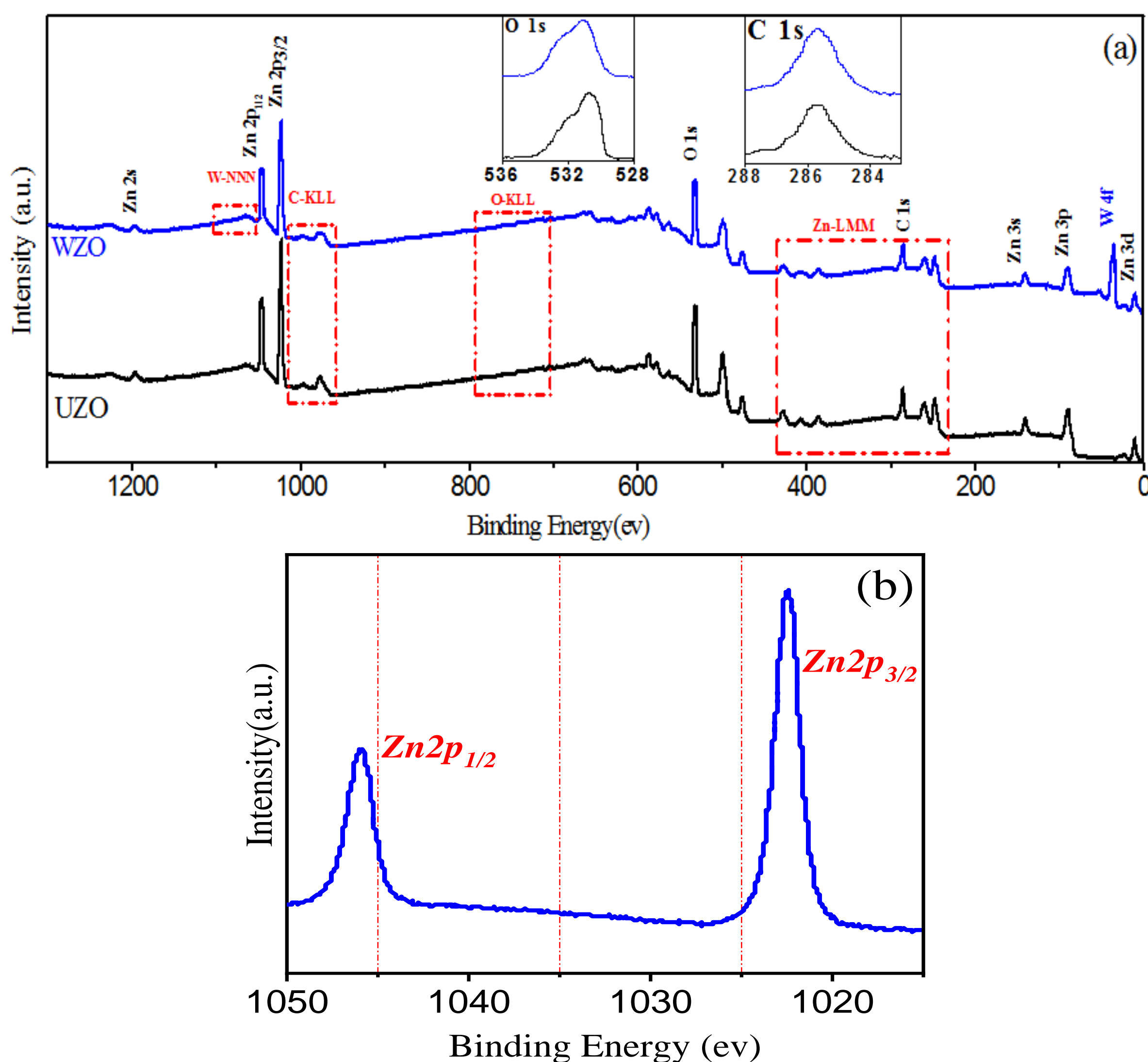

Fig. 2. (a) Survey of XPS core levels of UZO and WZO at the contaminated state (Zn3d, Zn 3p, Zn 3s, Zn 2p,C 1s, O1s) and (b) Zn2p split on two peaks with respective energy positions 1022.5 eV and 1045.5 eV (color online)

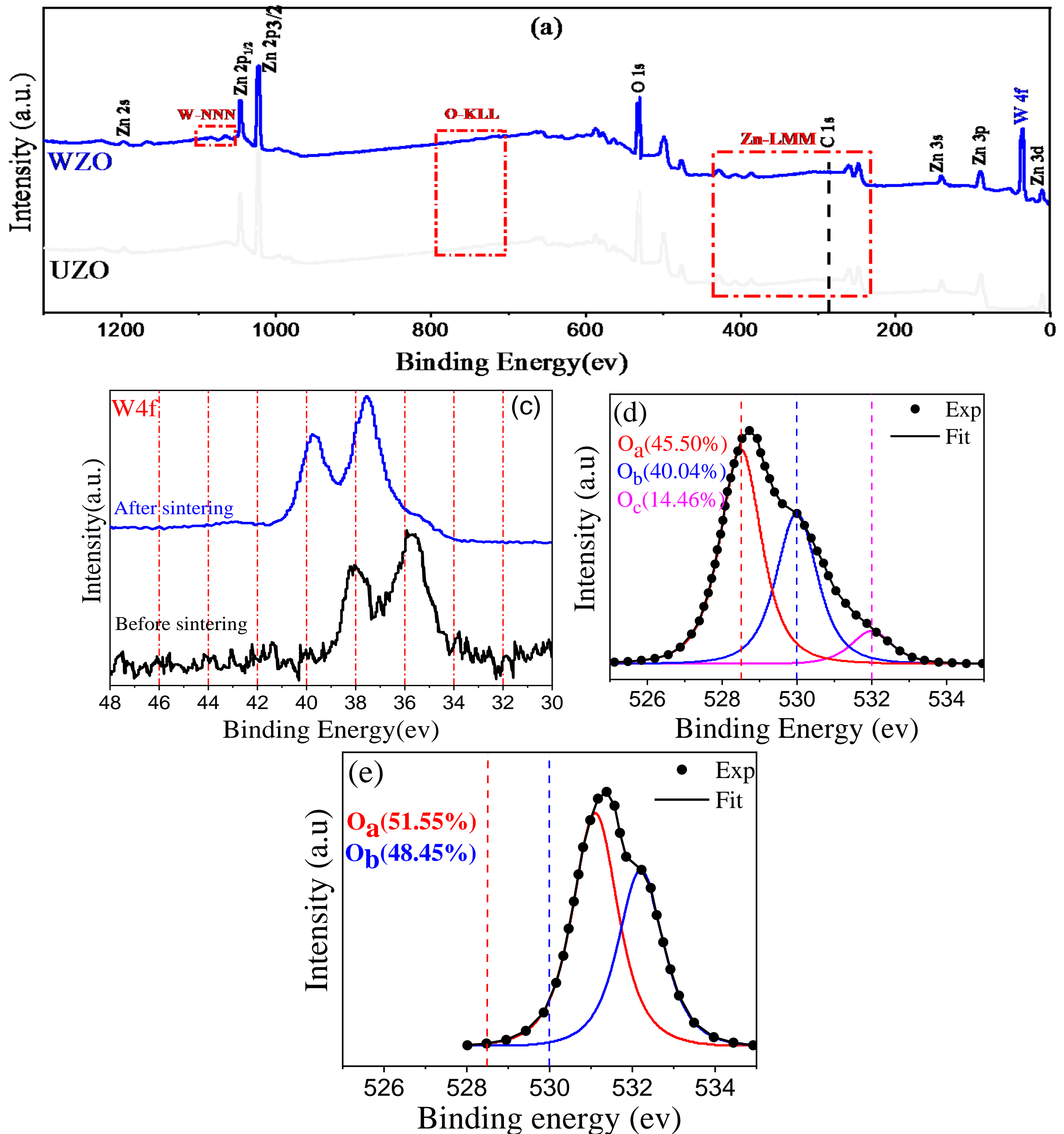

Fig. 3. XPS spectroscopy Survey (a). after heating and etching with W-NNN which appear at energies 1074 eV, (b) profiles of W4f for UZO and WZO. before and after heating , (c)and (d) :XPS spectroscopy deconvolution profiles of O1s of WZO before heating and etching and profiles of O1s of WZO after heating and etching (color online)

2.4. SEM characterization

Precise information regarding the chemistry and morphology of semiconductor surfaces is crucial for a wide range of applications, particularly in the study of their electrical, optical, and structural properties. Additionally, the influence of particle shapes and sizes and their performance evolution during physical treatments is of great interest due to its impact on the material's electrical and dielectric properties [57]. Scanning Electron Microscopy (SEM) is a valuable technique for achieving these objectives.

In this study, two SEM images were obtained using the JSM-6510 JEOL instrument under specific conditions [58]. The signal setting SEI was adjusted to 15 kV, with a working distance of 15 mm and a magnification range of 10000 to 1000000. Figs. 4a and 4b display the SEM images of the UZO and WZO samples, respectively, both grown on silicon substrates. The images were captured at a magnification of 50.000.

Upon observation, it is evident that the mean crystal sizes are 75 nm and 57 nm for UZO and WZO, respectively. These findings align with the decrease in particle sizes as indicated by the XRD spectroscopy results, further confirming the trend [59].

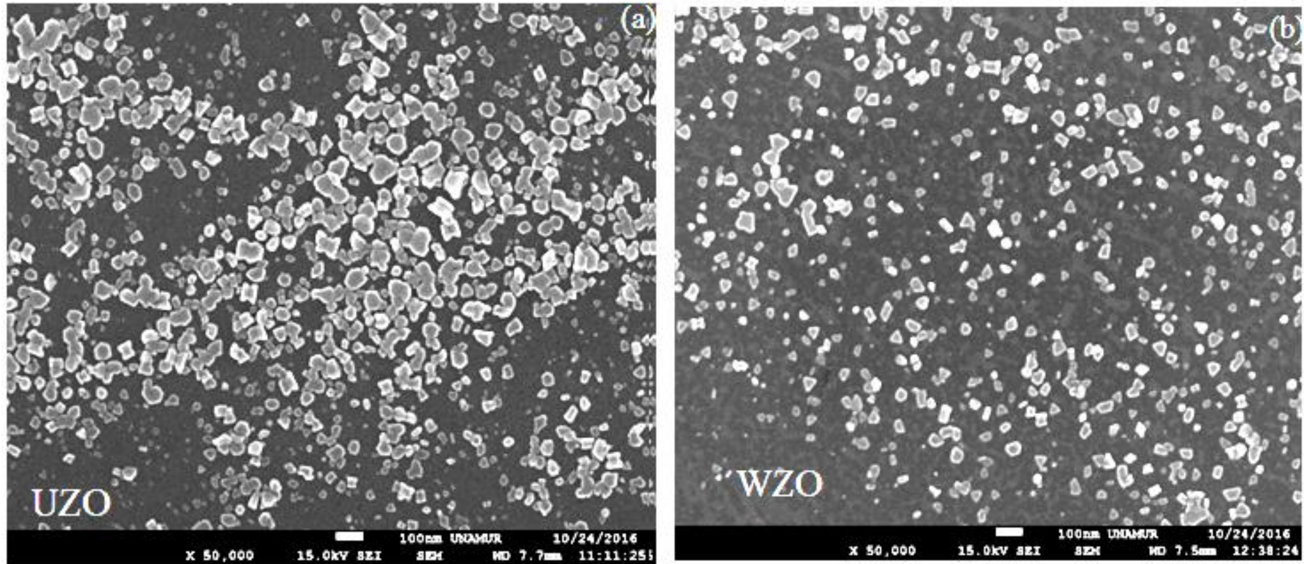

Fig. 4. Images obtained by the Scanning Electron Microscopy (SEM): (a) and (b) correspond respectively to the two Samples UZO and WZO

2.5. Electrical properties

The electrical properties of UZO and WZO were investigated through the fabrication of horizontal Schottky contacts. Gold metal, which possesses a higher work function than the electron affinity of ZnO (χZnO = 4.6 eV), was employed [60]. The experimental setup in Fig. 5d and inset 1 allowed for the characterization of several parameters. These included resistivity and conductivity as a function of the two samples' temperatures. Additionally, the setup allowed for the analysis of current-voltage (I–V), capacitance-voltage (C–V), conductance -voltage (σ-V), as well as real (ε'), and imaginary (ε") components of electrical permittivity. Various contact points have been rectified to avoid chemical reactions between the metal and the semiconductor (MIS). It is known that the formation of good ohmic contact is impeded by metal diffusion and the presence of Zn_i interstitial defects, Oi, and V_0 oxygen vacancies in the contact region. Additional procedures, such as chemical etching with HCl and oxygen treatment, followed by moderate-temperature heat treatment, are required to achieve ohmic contact [47, 60-68].

2.5.1. Electrical properties

The investigation of electrical properties in metal-insulator-semiconductor (MIS) systems, such as n-ZnO/p-Si with ZnO as the dielectric material, is of great interest [1, 2]. These properties rely on the conductivity provided by electrons in the conduction band and holes in the valence band of the ZnO crystal. This conductivity is directly influenced by the mobility of charge carriers. This mobility defines the efficiency of electric current conduction and the availability of carriers for transport, which in turn indicate the carrier concentration [69]. On the one hand, mobility is influenced by the phenomenon of free charge carriers' diffusion within the crystal [70]. To clarify these different conduction phenomena, measurements were performed using the SRM-RM 3000 Four-Point Probing System to accurately determine the resistivity.

Temperature variation was monitored using the Hewlett-Packard LF4192 impedance. With these devices, the variations of resistivity and conductivity as a function of temperature could be recorded, and the Arrhenius curve could be plotted using the following formula:

$$\sigma=\sigma_0 \exp\left(\frac{-E_a}{K_B T}\right) \tag{2}$$

where σ_0 is the conductivity factor's pre-exponential, $E_a$is the activation energy, K_B (1.3308 10^{-23}) is the Boltzmann constant, and T is the temperature in$(°K)$.

Three distinct regions can be observed. By plotting Ln(σ) as a function of T^{-1} in Fig. 5a, three activation energies were determined:

$$E_{aI} = (-0.83 \pm 0.02)eV, E_{aII}= (0.49 \pm 0.02)eV, E_{aIII}= (0.24 \pm 0.02)eV.$$

Ohmic contact was established as represented in Fig. 5b, by applying different voltages to the junction. With a fixed step of 0.3 V and a temperature of 60°C, the variations in current were recorded, reflecting the number of electron holes crossing the junction without

recombination. Fig. 5b displays the I-V characteristics of UZO and WZO. For the WZO characteristic, the current (I) begins to turn positive around a voltage of 0.6 V, indicating a P-N junction. Additionally, the WZO characteristic exhibits a more pronounced behavior compared to the UZO. Analysis of the current-voltage relationship suggests that the enhanced performance of the n-WZO/p-Si device is attributed to reduced recombination compared to ZnO. The determination of AC conductivity provides insights into the core of the semiconductor, where conductivity is relatively low, even though the conduction process is limited to the electrode [56].

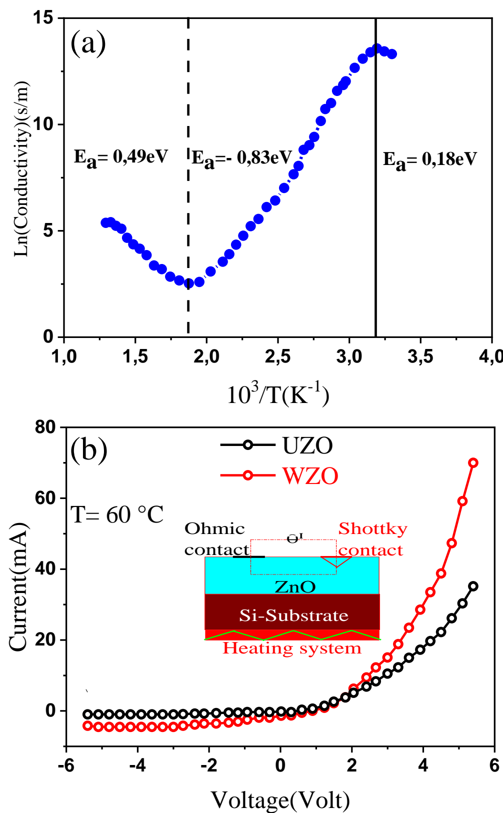

Fig. 5. ln (conductivity) (a) as function of temperature for WZO compound. and value of activation energies, (b) characteristics I-V for UZO and WZO (color online)

2.5.2. Conductance and capacitance

The dependencies of conductance and capacitance on frequency and temperature were measured using an AC generator over the frequency range of 10 Hz - 10 MHz. The variation of conductance σ (f) and capacitance C (f) as a function of frequency at room temperature is depicted in Fig. 6, with the frequency range set from 10 Hz to 1 MHz. It is observed that the conductance increases with increasing frequency, whereas the capacitance decreases with increasing frequency. Therefore, the maximum values of conductance 10^2 (Siemens) and capacitance 2.6 10^{-8}; 2 810^{-8}; 3.2 10^{-8}; and 2.6 10^{-8} (Farad) were recorded at 0.1 V, 0.2 V, 0.3 V, 0.4 V, and 0.5 V, respectively.

In this electrical investigation, the WZO/Si sample was obtained using tungsten-doped ZnO as an interface layer. The sample was subjected to capacitance–voltage (C–V) and conductance–voltage (σ/ω–V) measurements within the frequency range of 10 Hz to 10 MHz and a bias range of -6 volts to +6 volts at ambient temperature. The measurements were performed with a step size of 300 mV. In the metal-insulator-semiconductor (MIS) structure of the metal/n-WZO/p-Si junction, a potential V was applied between the ohmic and Schottky contacts. Indeed, three operating mechanisms were observed: accumulation, depletion, and an inversion layer [58, 59]. The application of a negative voltage causes the attraction of carriers toward the semiconductor's surface. Consequently, the density of holes on the thin semiconductor layer exceeds the density of electrons, resulting in surface inversion. As a result, the capacitance values increase in the accumulation region. Depletion and inversion regions are depicted in Fig. 7. Fig. 7b illustrates the variation of capacitances with voltage for different fixed frequencies on the frequency generator: 10 Hz, 100 Hz, 1 KHz, 10 KHz, 100 KHz, 1 MHz, and 10 MHz. In this figure, the C-V characteristics at 10 Hz exhibit a maximum capacitance (12 µF) in the accumulation region [71]. The obtained curves exhibit a similar overall profile, although there are variations in the maximum and minimum values. An increase in the capacitance maxima is observed in the accumulation region as the frequency decreases. The maximum value of the capacitance, 1.2 10^{-7} Farad, corresponds to the lowest frequency, f = 10 Hz, while the maximum value for the C-V curve observed at 10 MHz is approximately 6 10^{-8} Farad, which is half that amount. This increase in magnitude compared to the corresponding capacitance measured at 10 MHz in the depletion region can be attributed to the presence of ZnO-Si interface traps. In Fig. 7a, three operating mechanisms are observed for both fixed frequencies. An accumulation mechanism is identified at negative bias voltages below -2 V in the n-WZO/p-Si metal-insulator-semiconductor (MIS) structure, where the metal carries a negative electrical potential. The depletion of free charge carriers near the ZnO/Si interface in the semiconductor field is achieved in the range of -2V to -6V. The third region, at positive bias, corresponds to the formation of an inversion layer on the surface. The extended slope observed in the middle region of semiconductor depletion in the experimental curves can be attributed to the presence of charged traps near the ZnO/Si interface. The significant shift of the experimental curve towards negative voltages indicates the existence of fixed positive charges in the ZnO layer [72]. It is expected that the presence of tungsten elements will create a large number of holes in the n-WZO/p-Si interface. On the other hand, in Figs. 7c and 7d, the variations of the conductance (σ-V)and (σ/ω)-V) are recorded, respectively, under the same aforementioned conditions. The (σ/ω)-V characteristics exhibit three distinct mechanisms: accumulation, depletion, and inversion regions. Consistent with previous findings [71–73], it is observed that the values of (σ/ω) increase with increasing voltage in the negative voltage region, while they decrease with increasing frequency.

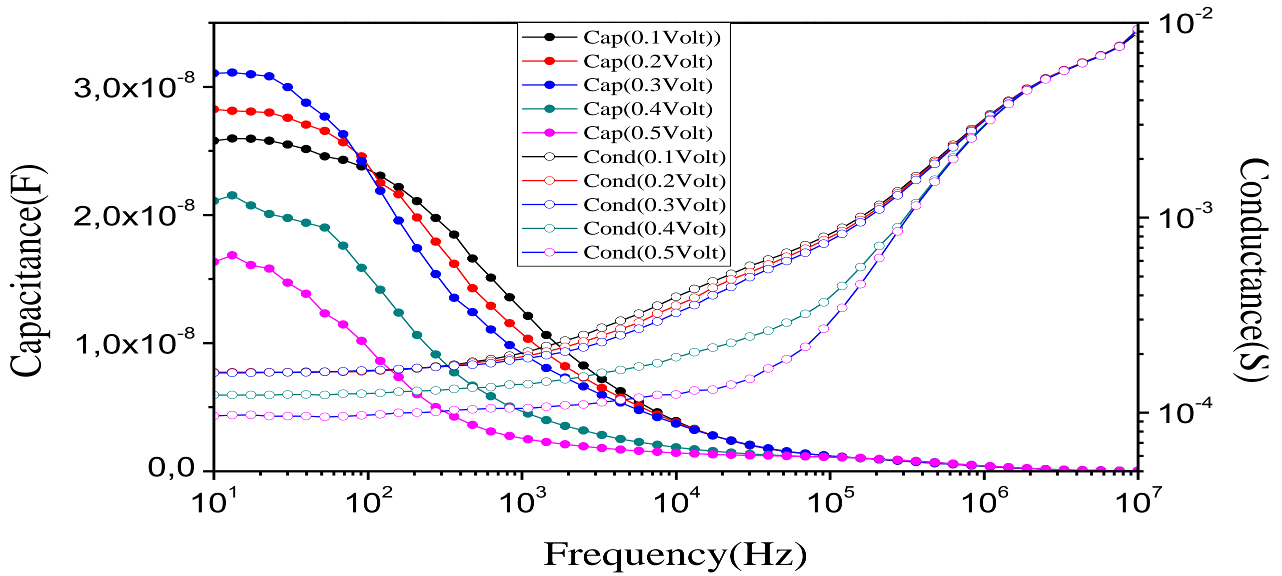

Fig. 6. The variation of conductance σ(f) and capacitance C(f) as function of frequency, at room temperature (color online)

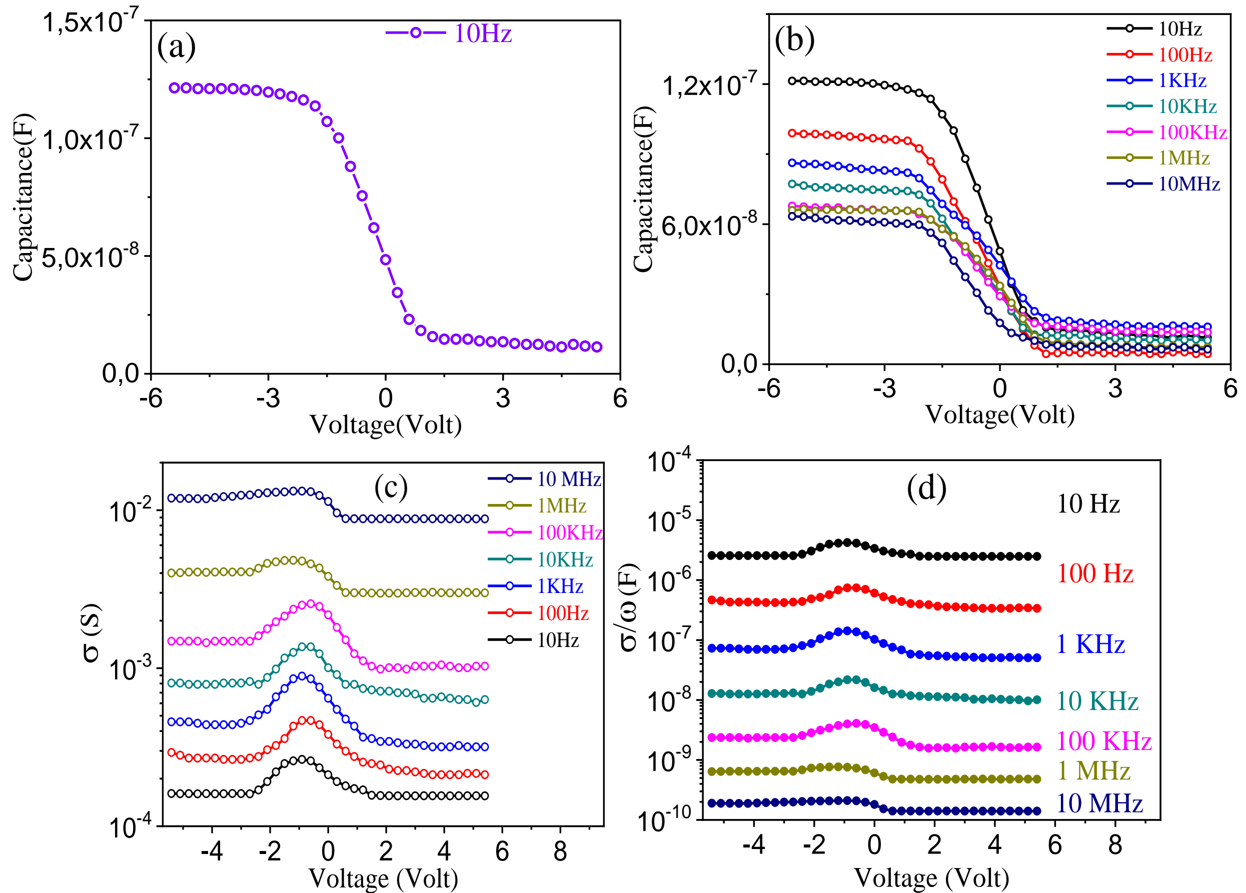

Fig. 7. Variation of capacitance C(V) (a) and (b) conductance σ(V) (c) and σ(V)/ω (d) as function of voltage for a frequency range 10Hz-10Mhz (color online)

2.5.3. Dielectric properties of WZO

The dielectric properties of WZO are typically characterized by the real component ε' and the imaginary component ε" of the electrical permittivity ε. These parameters, ε' and ε", can be determined directly from the measured conductance (σ_m) and capacitance (C_m) of the WZO material. The permittivity ε is calculated using the formula (3) [74].

$$\varepsilon = \varepsilon' - j\varepsilon = \frac{C_m}{C_0} - j\frac{\sigma_m}{\omega C_0} \quad (3)$$

Here, j is the complex number whose imaginary root is-1, and C_m and σ_m represent the measured capacitance and conductance, respectively. ω=2πf is the angular frequency. C_o is the capacitance of an empty capacitor. The capacitance of an empty capacitor, C_o can be calculated using formula (4) based on the contact area (A = 0.64 mm^2), the void permittivity (ε_o= 8.85 10^{-14} F/cm), and the thickness of the interfacial layer (d = 120 nm): [73].

$$C_o = \frac{\varepsilon_0 A}{d} \quad (4)$$

Using the measured values of $\frac{C_m}{C_0}$, and $\frac{\sigma_m}{\omega C_0}$, the real $\varepsilon'$and imaginary ε" were plotted in Fig. 8 a and b. It is observed that both the real and imaginarydielectric constants gradually decrease as the frequency of the WZO sample increases.

The application of the voltage induces an electric field, facilitating the migration of charge carriers inside the grains. Their accumulation at the grain boundaries forms a potential barrier, inducing an interfacial polarization [75]. The variation of voltage is similar to that of the capacitance for the real dielectric component ε' and follows the behavior of conductance for the imaginary dielectric component ε" of the electrical permittivity. The total electric permittivity is calculated based on the values of the real and imaginary components. Fig. 8c illustrates its variation with voltage at different fixed frequencies. In Fig. 8d, the variation of the dielectric constant with frequency is plotted for different applied voltages. In Fig. 8c,it can be observed that the dielectric constant exhibits three different mechanisms: accumulation, depletion, and inversion regions, following the behavior of capacitance. The maximum value of 891.39 is obtained at a frequency of 10 Hz, while the minimum value of 1.34 is reached at 10 MHz. In Fig. 8d, it is observed that the dielectric constant reaches important values (900 to 200) at low frequencies within the range of 10 Hz-100 Hz, but decreases dramatically as the frequency increases.

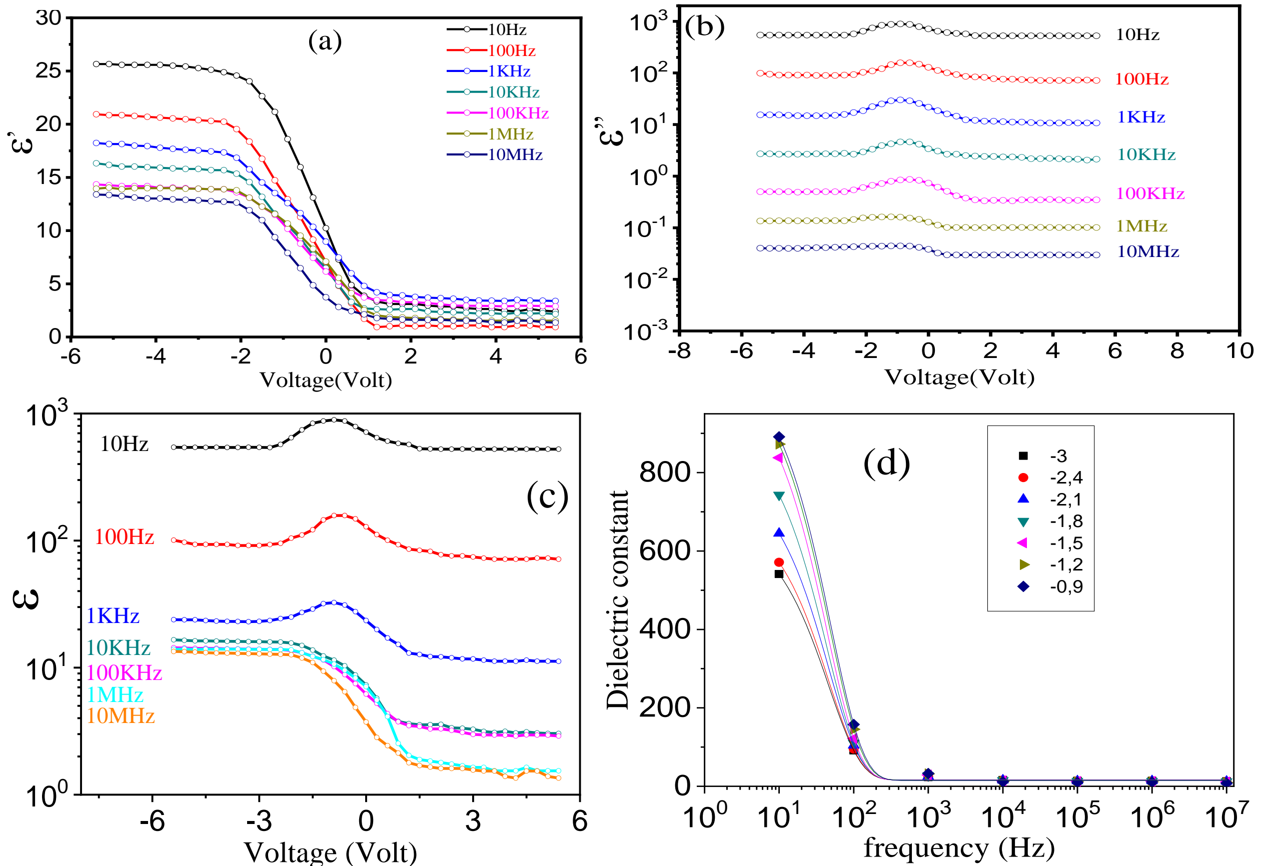

Fig. 8. (a) real ε' electrical permittivity, (b) imaginary ε" electrical permittivity,(c) dielectric constant as function of voltage and (d) dielectric constant as function of frequency ε for (A=64 mm² and d=120 nm of WZO material) (color online)

3. Conclusion

Pure ZnO and ZnO-doped tungsten with a proportion of 3% were synthesized using the spray pyrolysis technique. Their structural, electrical, dielectric, and morphological properties were investigated with XRD, XPS, SEM, four-probe methods, and network analyzers. It was observed, based on the XRD technique that the ZnO film exhibited orientation along the hkl (100) plane, and doping resulted in a decrease in crystal size. The electrical resistivity of the ZnO film, doped with 3% tungsten, decreased due to improved crystallinity, reduced grain size, and decreased grain boundaries. These results indicate an enhancement in the crystallinity of the doped ZnO film. The doped ZnO exhibited improved structural, electrical, and dielectric properties, making it suitable for applications such as gas sensing, radiation emission, and detection thanks to its surface area and high conductivity. Its favorable current-voltage, conductance-voltage, and capacitance-voltage characteristics make it promising for use in thin-film transistors. Additionally, the decrease in strain results in an increase in charge carriers and mobility, further supporting its applicability as a thin-film transistor. Finally, its high electrical conductivity makes it suitable for electrical energy storage applications.

References

[1] Xiyan Ding, Ke Lin, Yandong Li, L. Jiang, Journal of Cluster Science **31**, 1315 (2020).
[2] Mario Scuderi, Vincenzina Strano, Corrado Spinella, G. Nicotra, S. Mirabella, Nanotechnology **29**, 135707 (2018).
[3] Tobias Meißner, Kathrin Oelschla, Int. Nano Lett. **4**, 116 (2014).
[4] Norlida Kamarulzaman, Muhd Firdaus Kasim, Roshidah Rusdi, Nanoscale Research Letters **10**, 346 (2015).
[5] Lanli Chen, Yuanyuan Cui, Zhihua Xiong, M. Zhou, Y. Gao, RSC Adv. **9**, 21831 (2019).
[6] C. L. Hsu, K. C. Chen, T. Y. Tsai, T. J. Hsueh, Sensors and Actuators B **182**, 190 (2013).
[7] S. S. Mousavi, B. Sajad, M. H. Majlesara, Mater. Des. **162**, 249 (2019).
[8] Faiz Rahman. Optical Engineering **58**, 0109001 (2019)
[9] S. B. Bashar, M. Suja, M. Morshed, F. Gao, J. Liu, Nanotechnology **27**, 065204 (2016).
[10] S. M. Faraz, W. Shah, N. U. H. Alvi, O Nur, Q. U. Wahab, Condensed Matter Physics **2020**, 1 (2020).
[11] Khomdram Jolson Singh, Dhanu Chettri, International Conference on Inventive Communication and Computational Technologies (2017).
[12] J. Luo, Y. Wang, Q. Zhang, Sol. Energy **163**, 289 (2018)
[13] B. Deka Boruah, A. Misra, Nanoscale Adv. **8**, 18182 (2016)
[14] Z. Zhang, Q. Liao, Y. Yu, X. Wang, Y. Zhang, Nano Res. **9**, 237 (2014).
[15] Kavindra Kandpaland Navneet Gupta, Microelectronics International **35**, 52 (2018).
[16] K. Ravichandran, A. Jansi Santhosam, M. Sridharan, Surfaces and Interfaces **18**, 100412 (2020).
[17] L. Zhu, W. Zeng, Sensors and Actuators A **267**, 242 (2017).
[18] N. Izyumskaya, A. Tahira, Z. H. Ibupoto, N. Lewinski, V. Avrutin, U. Özgür, H. Morkoç, ECS State Sci. Technol. **6**, 84 (2017).
[19] S. Rajeshkumar, T. Lakshmi, P. Naik, Green Synthesis Characterization and Applications of Nanoparticles, Elsevier, ch. **18**, 445 (2019).
[20] X. He, J. E. Yoo, M. H. Lee, J. Bae, Nanotechnology **28**, 245402 (2017).
[21] D. Dimitrov, C. L. Tsai, S. Petrov, V. Marinova, D. Petrova, B. Napoleonov, S. ZH. Lin, Coatings **10**, 539 (2020).
[22] N. Siva, D. Sakthi, S. Ragupathy, V. Arun, N. Kannadasan, Materials Science and Engineering B **253**, 114497 (2020).
[23] Arindam Ghosh, Navniat Kumari, Ayon Bhattacharjee, Pramana Journal of Physics **84**, 621(2015).
[24] M. Bedrouni, B. Kharroubi, A. Ouerdane, M. H. Bouslama, Y. Caudano, K. B. Bensassi, M. Abdelkrim, Optical Materials **111**, 110560 (2021).
[25] Yulong Zhang, Weiyan Wang, Int. J. Appl. Ceram. Technol. **9**, 374 (2012)
[26] Senem Aydoğu, Seda Uzkalan, Journal of Science and Technology of Dumlupinar University **43**, 108 (2019).
[27] Chien-Yie Tsay, Wan-Yu Chiu, Coatings **10**, 1069 (2020).
[28] M. P. Dasari, U. Godavarti, V. Mote, Processing and Applications of Ceramics **12**, 100 (2018).
[29] D. B. Ruan, P. T. Liu, Y. C. Chiu, P. Y. Kuo, M. C. Yu, K. J. Gan, S. M. Sze, RSC Adv. **8**, 6925 (2018).
[30] O. Gen¸C. Yılmaz, F. Atayand, I. Akyuz, Modern Physics Letters B **30**, 1650171 (2016).
[31] Martin Chabicovsky, Miroslav Raudensky, Materiali in Tehnologije **49**, 337 (2015)
[32] Mohamed Guezzoul, Mohammed Bouslama, Abdellah Ouerdane, Azzeddine Mokadem, Bachir Kharroubi, Mahmoud Bedrouni, Mahfoud Abdelkrim, Abdelkader Abdellaoui, Kadda Benmokhtar Bensassi, Abdelhak Baizid, Mohamed Salah Halati, Applied Surface Science **520**, 146302 (2020).
[33] K. Baba, M. Nikravech, D. Vrel, Journal of Nanoscience and Nanotechnology **12**, 1 (2012).
[34] Fuxian Wang, AbdelkrimChemseddine, Fatwa F. Abdi, Roel van de Krol, Sean P. Berglund, J. Mater. Chem A **5**, 12838 (2017)
[35] Ananthu C. Mohan, B. Renjanadevi**,** Procedia Technology **24**, 761 (2016).
[36] C. K. Choi, C. Y. Kim, H. S. Lee, J. K. Woo, R. Navamathavan, K. M. Lee, M. T. Hyun, Journal of the Korean Physical Society **57**, 1976 (2010).
[37] E. F. Keskenler, M. Tomakin, S. Doğan, G. Turgut, S. Aydın, S. Duman, B. Gürbulak, Journal of Alloys and Compounds **550**, 129 (2013).
[38] Ali Can Güler, Bircan Dindar, Hümeyra Örücü,

Materials Research Express **6**, 065017 (2019).
[39] X. A. Zhang, F. Hai, T. Zhang, C. Jia, X. Sun, L. Ding, W. Zhang, W., Microelectronic Engineering **93**, 5 (2012).
[40] K. Omri, I. Najeh, L. El Mir, Ceramics International **42**, 8940 (2016).
[41] K. Yim, J. Lee, D. Lee, M. Lee, E. Cho, H. Lee, S. Han, Scientific Reports **7**, 40907 (2017).
[42] Didik Aryanto, Erna Hastuti, Melda Taspika, Khoirul Anam, Isnaeni Isnaeni, Wahyu B Widayatno, Agus S Wismogroho, Putut Marwoto, Bebeh W Nuryadin, Alfian Noviyanto, Sugianto Sugianto, Journal of Sol-Gel Science and Technology **96**, 226 (2020).
[43] Peng Chen, Matthew Baldwin, Prabhakar R. Bandar, The Royal Society of Chemistry **5**, 14898 (2017).
[44] M. Sahal, B. Marí, M. Mollar, F. J. Manjón, Phys. Status Solidi C **7**, 2306 (2010).
[45] A. Kumar, A. Sharma, S. Bhasker, R. P. Yadav, H. P. Bhasker, P. K. Priya, R. K. Anand, Mater. Res. Express **6**, 115039 (2019).
[46] K. Pradeev Raj, K. Sadaiyandi, A. Kennedy, S. Sagadevan, Z. Z. Chowdhury, M. R. BinJohan, R. RathinaBala, Nanoscale Research Letters **13**, 229 (2018).
[47] E. Muchuweni, T. S. Sathiaraj, H. Nyakotyo, Heliyon **3**, e00285 (2017).
[48] M. Rabiei, A. Palevicius, A. Monshi, S. Nasiri, A. Vilkauskas, G. Janusas, Nanomaterials **10**, 1627(2020).
[49] Y. Benkhetta, A. Attaf, H. Saidi, A. Bouhdjar, H. Benjdidi, I. B. Kherchachi, N. Lehraki, Optik **127**, 3005 (2016).
[50] M. H. Hong, H. Choi, D. I. Shim, H. H. Cho, J. Kim, H. H. Park, Solid State Sciences **82**, 84 (2018).
[51] J. K. Saha, R. N. Bukke, N. N. Mude, J. Jang, Nanomaterials **10**, 976 (2020).
[52] Katsushi Kishimoto, Yoshitaro Nose, Yasuaki Ishikawa, Mami N. Fujii, Yukiharu Uraoka, Journal of Alloys and Compounds **672**, 413 (2016).
[53] R. Ji, D. Zheng, C. Zhou, J. Cheng, J. Yu, L. Li, Materials **10**, 820 (2017).
[54] Martin Köppen, Condensed Matter **4**, 82 (2019).
[55] T. Wagner, D. Valbusa, L. Bigiani, D. Barreca, A. Gasparotto, C. Maccato, Surf. Sci. Spectra **27**, 024004 (2020).
[56] John F. Moulder, William F.Stickle, Peter E. Sobol, Kenneth D. Bomben, Handbook of X-ray photoelectron spectroscopy, Perkin Elmer corporation Physical electronic division, 1992.
[57] Oleg Ivanov, Oxana Maradudina, Roman Lyubushkin, Materials Characterization **99**, 175 (2015).
[58] JEOL, Basic knowledge for using the SEM, https://www.jeol.co.jp/en/applications/pdf/sm/sem_atoz_all.pdf
[59] H. Ji, Z. Cai, W. Pei, X. Huang, Y. Lu, Journal of Materials Research and Technology **9**, 4340 (2020).
[60] Leonard J. Brillson, Yicheng Lu, J. Appl. Phys. **109**, 121301 (2011)
[61] J. H. Kang, A. Song, T. J. Park, J. H. Seo, B. Walker, K. B. Chung, K. B, Polymers **12**, 737 (2020).
[62] Buket Akin, Semsettin Aldindal, Journal Pre-Proof Physica B **594**, 412274 (2020).
[63] S. A. Sundar, N. J. John, International Journal of Engineering and Applied Sciences **3**, 257706 (2016).
[64] B. Shen, H. Wang, S. Li, J. H. Gong, Key Engineering Materials **492**, 250 (2012).
[65] H. K. Jang, Y. D. Chung; S. W. Whangbo, I. W. Lyo, C. N. Whang, S. J. Lee, Seok Lee, Journal of Vacuum Science & Technology A Vacuum Surfaces and Films **18**, 2563 (2020).
[66] Oleg Ivanov, Oxana Maradudina, Roman Lyubushkin, Materials Characterization **99**, 175 (2015).
[67] M. F. Nasir, M. Hannas, M. H. Mamat, M. Rusop, Advanced Material Research **1109**, 572 (2015).
[68] A. Nikravan, Y. Badali, Ş. Altındal, İ. Uslu, İ Orak, Journal of Electronic Materials **46**, 5728 (2017).
[69] R.Ben Belgacem, M. Chaari, A. F. Braña, B. J. Garcia, A. Matoussi, Journal of the American Ceramic Society **100**, 2045 (2017).
[70] I. Hussain, M. Y. Soomro, N. Bano, O. Nur, M. Willander, Journal of Applied Physics **112**, 64506 (2012).
[71] Yocef Baladi, Semsettin Aldindal, Ibrahim Uslu, Materials International **28**, 325 (2018).
[72] R. Ondo-Ndong, H. Essone-Obame, Z. H. Moussambi, N. Koumba, Journal of Theoretical and Applied Physics **12**, 309 (2018).
[73] A. Buyukbas-Ulusan, İ. Taşcıoğlu, A. Tataroğlu, F. Yakuphanoğlu, S. Altındal, Journal of Materials Science: Materials in Electronics **30**, 12122 (2019).
[74] S. A. Yerişkin, G. E. Demir, İ. Yücedag, Journal of Nanoelectronics and Optoelectronics **14**, 1126 (2019).
[75] A. Modwi, K. K. Taha, L. Khezami, A. S. Al-Ayed, O. K. Al-Duaij, M. Khairy, M. Bououdina, Journal of Inorganic and Organometallic Polymers and Materials **30**, 2633 (2020)

*Corresponding author: z.hachemi@univ-dbkm.dz; zehar.elhachemi@yahoo.com